Energy Storage Materials 49 (2022) 85–92

Contents lists available at ScienceDirect

Energy Storage Materials

journal homepage: www.elsevier.com/locate/ensm

Precisely visit the performance modulation of functionalized separator in Li-S batteries *via* consecutive multiscale analysis

Zhangxiang Hao[a,b,#], Jie Chen[c,#], Xuekun Lu[d], Liqun Kang[b], Chun Tan[d], Ruoyu Xu[b], Lixia Yuan[c,*], Dan J.L. Brett[d,e], Paul R. Shearing[d,e,*], Feng Ryan Wang[b,*], Yunhui Huang[c,*]

[a] School of Science, School of Chip Industry, Hubei University of Technology, Wuhan, Hubei 430068, China
[b] Materials and Catalysis Laboratory, Department of Chemical Engineering, University College London, London WC1E 7JE, United Kingdom
[c] School of Materials Science and Engineering, Huazhong University of Science and Technology, Wuhan, Hubei 430074, China
[d] Electrochemical Innovation Lab, Department of Chemical Engineering, University College London, London WC1E 7JE, United Kingdom
[e] The Faraday Institution, Quad One, Harwell Science and Innovation Campus, Didcot OX11 0RA, United Kingdom

ARTICLE INFO

Keywords:
Precisely visit
Performance modulation
Functionalized separator
Li-S batteries
Consecutive multiscale analysis

ABSTRACT

Despite progress of functionalized separator in preventing the shuttle effect and promoting the sulfur utilization, the precise and non-destructive investigation of structure-function-performance associativity remains limited so far in Li-S batteries. Here, we build consecutive multiscale analysis *via* combining X-ray absorption fine structure (XAFS) and X-ray computational tomography (CT) techniques to precisely visit the structure-function-performance relationship. XAFS measurement offers the atomic scale changes in the chemical structure and environment. Moreover, a non-destructive technique of X-ray CT proves the functionalized separator role for microscopic scale, which is powerful chaining to bridge the chemical structures of the materials with the overall performance modulation of cells. Benefiting from this consecutive multiscale analysis, we report that the uniform doping of Sr^{2+} into the perovskite $LaMnO_{3-\delta}$ material changes the Mn oxidation states and conductivity (chemical structure), leading to effective lithium polysulfide trapping and accelerated sulfur redox (separator function), and resulting in outstanding cell performance.

1. Introduction

Lithium-sulfur (Li-S) batteries are among the most promising candidates for next-generation electrochemical devices due to the high specific theoretical capacity (1672 mAh g^{-1}) and the use of earth-abundant element sulfur [1–6]. Currently, the practical application of Li-S battery technology is limited by low sulfur utilization and severe shuttle effects, which are caused by the low electronic conductivity of the sulfur species (S_8/Li_2S_2/Li_2S) and the dissolution of intermediate polysulfides (Li_2S_x, $3 \leq x \leq 8$) during the cathode process [7–11]. In addition, these limitations escalate at high and realistic sulfur loadings. Tremendous effort has been made to enhance the electrochemical stability of the sulfur cathode and to effectively overcome the shuttle phenomenon. One efficient route is to use a functional separator to increase sulfur utilization efficiency, improve redox kinetics and physically shield the diffusion of Li_2S_x to the anode [12,13]. While research has been predominantly focused on carbon and polymer modified functional separators [14–21], metal oxides [22–26] have arisen recently as conductive and polar-functional modifier due to their unique advantages in: 1) chemical shielding of the diffusion of polysulfides, and 2) reactivating inactive deposits of sulfur-containing species. It is therefore important to rationalize how the chemical structure improvement at atomic scale leads to the superior function (1 and 2) above, and finally to the increase of battery storage capacity. This is a multi-scale problem that involves atoms, microstructures, and overall cell performance, calling for a consecutive multiscale analysis.

The chemical shielding of polysulfides and reactivation of sulfur deposits occur at microscopic scale during the charge and discharge of the battery, while the chemical modification of the separator happens at atomic scale. Lack of the non-destructive probing method in validating those functions is the bottleneck in understanding the structure-function-performance relations. Currently, the study of chemical shielding effect is limited to *ex situ* UV-vis observation of colour change in polysulfide solution when applying the separator [27–33], and the U-type polysulfide diffusion [15,34] experiment to simulate the diffusion of lithium polysulfides through the separator. The behaviours of the separator in the assembled battery remains an unexplored black box. Here we couple the X-ray Computed Tomography (CT) with X-ray absorption fine structure (XAFS) to rationalize the structure-function relation of the

* Corresponding authors.
E-mail addresses: yuanlixia@hust.edu.cn (L. Yuan), p.shearing@ucl.ac.uk (P.R. Shearing), ryan.wang@ucl.ac.uk (F.R. Wang), huangyh@hust.edu.cn (Y. Huang).
# These authors contributed equally to this work.

https://doi.org/10.1016/j.ensm.2022.04.003
Received 19 November 2021; Received in revised form 31 March 2022; Accepted 1 April 2022
Available online 4 April 2022
2405-8297/© 2022 The Author(s). Published by Elsevier B.V. This is an open access article under the CC BY license (http://creativecommons.org/licenses/by/4.0/)

separator. X-ray CT is a non-destructive imaging method at microscopic scale to acquire high-spatial resolution three-dimensional (3D) images [35–39] of complete cell before and after charge/discharge cycles. This enables three-dimensional image analysis to quantify microstructural evolution processes, facilitating the identification of potential failure and degradation mechanisms [40,41]. XAFS studies the average oxidation state of metal cations and their location coordination environment of the modified separator, providing the insight into the atomic and electronic structures. The coupling of XAFS-CT analysis here is the first time for energy storage systems.

In the design of functional separator, we successfully dope Sr^{2+} of 0.3 molar ratio into a perovskite-type $LaMnO_3$ membrane, showing highest electronic conductivity and positive polysulfide adsorption effect, then further validate its function in shielding polysulfide that leads to the increase of the storage capacity *via* above-mentioned consecutive multi-scale technique containing XAFS, Scanning Transmission Electron Microscopy (STEM), X-ray CT and electrochemical performance. XAFS technique reveals the oxidation state increase of Mn, forming Mn^{3+}/Mn^{4+} pair with weak John Teller effect that leads to high conductivity, which can help the electron transfer with high loading cathode to improve the cell performance. As a result, high electron hopping conduction of 28.61 S cm^{-1} for Sr^{2+} doping (0.3 molar ratio) compared to 0.15 S cm^{-1} for pristine $LaMnO_3$ is achieved. Non-destructive 3D X-ray CT offers the visualized evidence of polysulfide diffusion before and after cycles, revealing how to block the polysulfide shuttle effect through Sr-doping modified separator. Benefiting from both high conductivity and excellent trapping ability, Li-S batteries with $La_{0.7}Sr_{0.3}MnO_{3-\delta}$ (LSMO-0.3) modified separator delivers a high reversible capacity of 932 mAh g^{-1} and outstanding cycle stability with only 0.2% capacity fade per cycle over 300 cycles at a high sulfur loading of 6.9 mg cm^{-2}.To the best of our knowledge, it is the first time to reveal that a sub-nanometre change of the materials (radius of the Sr^{2+} is 118 pm) can lead to the significant performance improvement of a 20 mm cell. Our study provides new insight into how the atomic-level structure and properties of materials affect microscopic scale membrane changes observed by state-of-the-art XAFS, X-ray CT and simulation technique, and further lead to the enhancement of overall electrochemical performance.

2. Experimental section

2.1. Fabrication of LMSO-0.3 modified and LMO-modified separator

$La_{0.7}Sr_{0.3}MnO_{3-\delta}$ powder was fabricated via a classic sol-gel method. In a typical process, 1.516 g $La(NO_3)_3{\cdot}6H_2O$ (Sinopharm Chemical Reagent Co., Ltd.), 0.317 g $Sr(NO_3)_2$ (Sinopharm Chemical Reagent Co., Ltd.), 1.255 g $Mn(NO_3)_2{\cdot}4H_2O$ (Sinopharm Chemical Reagent Co., Ltd.) and 1.260 g citric acid monohydrate (Sigma-Aldrich) were dissolved in 30 mL deionized water. Then, the solution was evaporated at 80 °C under stirring for 12 h to obtain the yellow precursor. Finally, the precursor was pre-sintered at 400 °C for 3 h and sintered at 800 °C for 2 h in the atmosphere to obtain the LSMO-0.3 powder. The $La_{1-x}Sr_xMnO_{3-\delta}$ powder (x=0-0.5) was fabricated by the same method with different stoichiometric ratio. The LSMO-0.3 modified separator was prepared by mixing 60 wt.% LSMO-0.3, 30 wt.% super P, and 10 wt.% polyvinylidene difluoride (PVDF) in N-Methyl pyrrolidone (NMP) to form a homogeneous slurry. This slurry was coated on one side of a commercial Celgard separator with a glass rod, and then dried in an oven at 80 °C for 6 h. After drying, the LSMO-0.3 modified separator was cut into wafers with a diameter of 18 mm for cell assembly. The LMO-modified separator was fabricated via the same method with the reactants 2.165 g $La(NO_3)_3{\cdot}6H_2O$, 1.255 g $Mn(NO_3)_2{\cdot}4H_2O$, and 1.260 g citric acid monohydrate.

When the stoichiometry of Sr-doping exceed 0.5, higher temperatures are required for phase-pure fabrication, which leads to larger paricles compared to stoichiometry of Sr-doping below 0.5 [44]. So the $La_{1-x}Sr_xMnO_{3-\delta}$ (x=0-0.5) was selected in this work because smaller particles can offer more adsorption positions which promotes the effect of functional membrane.

2.2. Electrochemical measurements

All the electrochemical measurements were tested using 2032 coin cells with Li foil as anode, and the electrolyte consists of 1 M lithium bis(trifluoromethanesulfonyl)imide (LiTFSI) in a mixed solution of 1, 2-dimethoxyethane (DME) and 1, 3-dioxolane (DOL) (1:1 v/v) with $LiNO_3$ (2 wt.%). The sulfur cathode was prepared by mixing commercial sulfur powder, super P, LA133 in a weight ratio of 65: 25: 10 in deionized water. The slurry was coated on aluminum (Al) foil (S loading below 3 mg cm^{-2}) or carbon paper (S loading above 3 mg cm^{-2}), and then dried at 80 °C overnight in an oven. The mass of carbon paper is about 4.1 mg cm^{-2}, which is similar to the Al foil current. Finally, the electrode was punched into round discs with a diameter of 8 mm. The mass loading in the cathode ranges between 2-8.5 mg cm^{-2}. The loading of coating on the separator is about 0.75 mg cm^{-2}. The ratio of sulfur to electrolyte is 0.05 mg μL^{-1} for all the cells. The CV measurement was conducted on an electrochemical workstation (CHI614b) at a scan rate of 0.05 mV s^{-1} with a voltage range of 1.7-2.8 V at room temperature. All galvanostatic charge and discharge tests were performed with a voltage window of 1.7-2.8 V on a battery measurement system (Land, China).

2.3. Characterization

XRD patterns were obtained using a lab-based diffactometer (Holland, PANalytical X'pert PRO-DY2198) with the X-ray source set to 40 mA and 40 kV, using characteristic Cu Kα radiation. The structure and morphology of LSMO were measured using SEM (Sirion 200, FEI, USA). Bright Field (BF) and High Angle Annular Dark Field (HAADF) STEM images were acquired on probe-corrected (CEOS) Scanning Transmission Electron Microscope (JEM ARM 200CF, JEOL, Japan) at 200 kV acceleration voltage. Energy-Dispersive X-ray Spectroscopy (EDS) and elemental mapping data were obtained on the same microscope. The Brunauer-Emmett-Teller (BET) surface area was calculated according to the adsorption data in the relative pressure range of 0.06 to 0.2. The conductivity is tested by 4-point probe method. The LSMO-0.3/Li_2S_4 chemicals prepared from the visual adsorption experiments in supplementary Fig. 11 after 12 h. The LSMO-0.3/Li_2S_4 samples are dried in the glovebox and transferred to XPS while sealing with Ar gas. XPS analysis was conducted with a Kratos Analytical spectrometer (AXIS ULTRA DLD-600W) and Al Kα (1486.6 eV) X-ray source, and the binding energy values were calibrated by the C 1s peak at 285.0 eV.

XAFS spectra of Mn K-edge, Sr K-edge, La L_3-edge and L_1-edge were acquired at Beamline B18 of the Diamond Light Source (UK). All measurements were performed in transmission mode using a QEXAFS setup consisting of a Si (111) double crystal monochromator and ionisation chamber detectors. Mn foil, La_2O_3 and SrO standards were used for energy shift calibration. The $La_{1-x}Sr_xMnO_{3-\delta}$ (x=0-0.5) sample powder was diluted with boron nitride and pressed into a 8 mm diameter pellet for measurement. XAFS data was analysed using Demeter software. The amplitude reduction factors ${S_0}^2$ of Sr K-edge and Mn K-edge were calculated to be 1.00 and 0.65 from EXAFS analysis of SrO and Mn foil and used as a fixed parameter for EXAFS fitting.

The Near Edge X-ray Absoprtion Fine Structure (NEXAFS) measurement was accomplished at the ISISS beamline of BESSY II (Germany). NEXAFS spectra at Mn L_3/L_2 edge and O K-edge were measured in total electron yield (TEY) mode under UHV condition (600l/mm plane grating monochromator, 111 μm slit size, cff =2.25).

2.4. X-ray micro-CT

The bespoke Swagelok cell was assembled as the same components as the aforementioned coin cells with electrode and carbon-coated Al foil of 2.5 mm diameter, which is suitable for the X-ray transmission. This

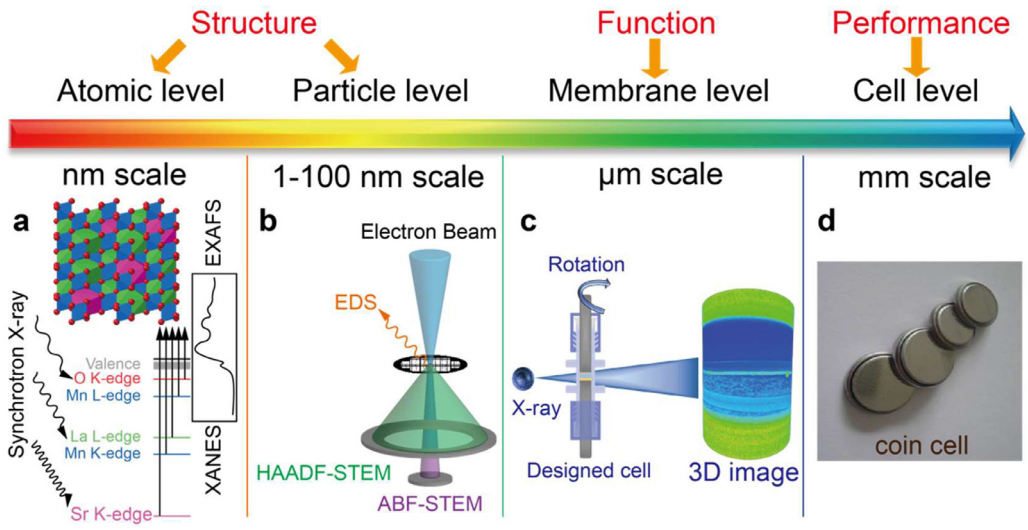

Fig. 1. Schematic illustration of consecutive multi-scale investigations with (a) XAFS, (b) STEM, (c) X-ray micro CT and (d) whole cell, in order to achieve the structure-function-performance relationship.

bespoke Swagelok cell was assembled and imaged before and after cycling on a Zeiss Xradia Versa 520 X-ray microscope operated at a source voltage of 100 kV (Carl Zeiss XRM, CA, USA). The source-to-sample and sample-to-detector distances were set to 16 and 14 mm, respectively, and when combined with 40 × optical magnification, resulted in a voxel size of 0.36 μm and a field-of-view (FOV) of 360 × 360 μm^2. X-ray projections were collected every 30 s in even angular steps over 360° of rotation, equivalent to a step size of 0.15° and a total of 2401 projections. These radiographic projections were then reconstructed by a proprietary Feldkamp-Davis-Kress (FDK) algorithm in the Zeiss Xradia XMReconstructor software. Images segmentation and volume fraction analysis of the electrode component was conducted using Avizo 9.4 (Thermo Fisher Scientific, UK). The thickness of different electrode layers was quantified using a MATLAB script by counting the constitutive voxels of the segmented data in the depth direction.

3. Results and discussion

3.1. Multiscale methodology

The relationship of material structure, function and performance is investigated *via* consecutive multi-scale techniques (Fig. 1). XAFS probes the local coordination environment and chemical state of Sr^{2+} and $Mn^{3+/4+}$ within a few angstroms (Å) (Fig. 1a). STEM confirms the uniform doping of the Sr^{2+} across the whole $La_{1-x}Sr_xMnO_{3-\delta}$ (LSMO) particle (Fig. 1b). The X-ray micro-CT validates the chemical shielding function of Sr doped LSMO separator (Fig. 1c). The cell performance is then evaluated to establish the structure-function-performance relationship (Fig. 1d). This consecutive multiscale analysis can precisely visit the performance modulation of functionalized separator in Li-S batteries.

3.2. The $La_{1-x}Sr_xMnO_{3-\delta}$ atomic structure

The perovskite-type $La_{1-x}Sr_xMnO_{3-\delta}$ (LSMO) has controllable chemical component, cation valence, oxygen vacancy and high chemical stability, which can be flexibly designed to work out the issues in lithium-sulfur batteries. The X-ray diffraction (XRD) patterns of $La_{1-x}Sr_xMnO_{3-\delta}$ (x=0-0.5) show crystallized phase (Supplementary Fig. 1). The diffraction peaks match well with the rhombohedral lattice with space group $R\bar{3}c$ (JCPDS no. 86-1230). The lattice slightly shrinks to smaller lattice parameters with higher Sr doping.

XAFS analysis over Mn K, L_3-edge, Sr K-edge, La L_3-edge and O K-edge is carried out to obtain the complete structure information, including oxidation states, electronic structure and the local coordination environment of $La_{1-x}Sr_xMnO_{3-\delta}$ at the atomic scale. Divalent Sr^{2+} replaces the trivalent La^{3+} at the same position in the lattice regardless of Sr loading, as determined from the X-ray absorption near edge spectroscopy (XANES) and extended X-ray absorption fine structure (EXAFS) (Supplementary Fig. 2-4 and supplementary Table 1). Both the bulk and surface oxidation states of Mn are increased upon Sr^{2+} doping, as shown in the blue shifts of white line position for Mn K-edge and $L_{3,2}$-edge XANES, respectively (Fig. 2a,b, supplementary Fig. 5). All the absorption edges lie between the Mn^{3+} in Mn_2O_3 and Mn^{4+} in MnO_2, indicating the average valence of Mn in LSMO is between +3 and +4. The characteristic shoulder peak A (Fig. 2b) contained in all LSMO sample is also corresponding to Mn^{4+} absorption feature [42–44], thus we confirm the transition from Mn^{3+} to Mn^{4+} during Sr^{2+} doping. The average Mn-O coordination number remains at 6.0 ± 0.2 upon Sr doping (Fig. 2c, supplementary Fig. 6 and supplementary Table 2). The decrease of the scattering feature at 3.38 Å suggests the substitution of La by Sr. The Mn-O-Mn scattering appears at 3.92 ± 0.01 Å, corresponding MnO_6 octahedrons connected *via* one O vertex. The coordination number of both Sr-O and Sr-Mn is very close to the theoretical value of 12 and 8. The Sr-Mn distance decrease with higher Sr doping, which is consist of the shrink of lattice and shift of XRD diffraction peaks (Fig. 2d, supplementary Fig. 1, 2 and supplementary Table 1).

The origin of conductivity in the perovskite stems from electron hopping conduction [45]. In the case of $Mn^{3+}/^{4+}$ pair, the electron hops from Mn^{3+} to Mn^{4+} in two neighbouring MnO_6 octahedra *via* the linear shape Mn^{3+}-O-Mn^{4+} orbital overlap ($3d_z{}^2$ and $2p_z$) (Fig. 2). The probability of such hopping conduction is depended on the ratio of Mn^{3+}/Mn^{4+} and the Jahn-Teller distortion of the Mn(III)O_6 octahedrons (Fig. 2e), both of which can be modified by Sr doping in the $La_{1-x}Sr_xMnO_{3-\delta}$ system. The probability of electron hopping is studied *via* O K-edge Near edge X-ray absorption fine structure. Two absorption features are found at 529.5 eV and 532 eV (Fig. 2f), corresponding to the electron transition from O 1*s* to the $e_g \uparrow + t_{2g} \downarrow$ orbitals (green) and $e_g \downarrow$ orbital (yellow) in the O 2*p* and Mn 3*d* hybridization (The ↑ and ↓ suggest the final spin state of the excited O 1s electron) [46]. According to the literature, materials with weak Jahn-Teller distortion of Mn^{3+} that leads to similar energy levels of Mn^{3+} $e_g \uparrow$ ($3d_z{}^2$), Mn^{4+} $e_g \uparrow$ ($3d_z{}^2$) and O $2p_z$ will have high conductivity. Such weak Jahn-Teller distortion is shown in a small full width half maximum (FWHM) of the O 1*s* to the $e_g \uparrow$ and $t_{2g} \downarrow$ transition (Fig. 2f green) [46]. From 0.1 to 0.5 Sr-doping, the FWHM drops to the minimum at 0.3 Sr and slightly increases afterwards (Fig. 2g red). Accordingly, the conductivity increases

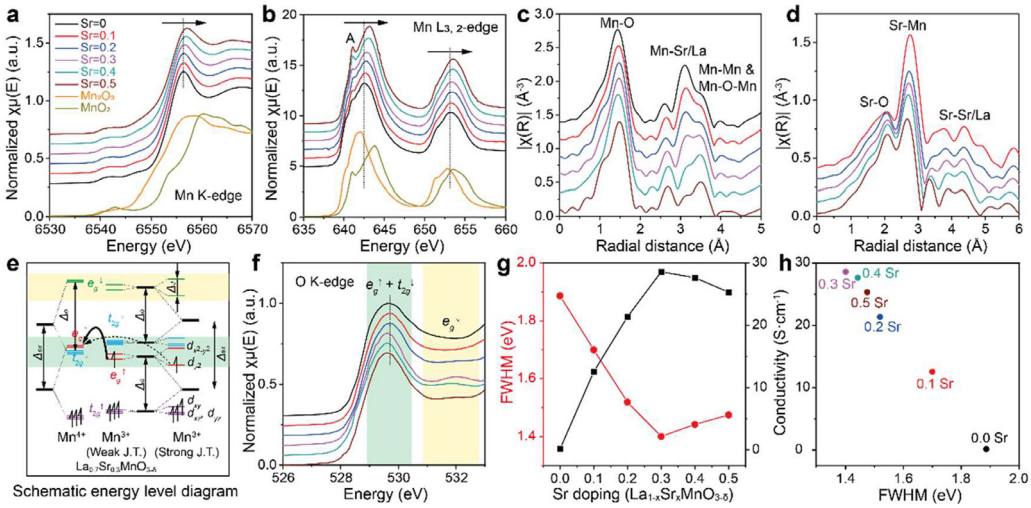

Fig. 2. Characterization of $La_{1-x}Sr_xMnO_{3-\delta}$ (x=0~0.5). (a) XANES spectra of $La_{1-x}Sr_xMnO_{3-\delta}$ at Mn K-edge. (b) NEXAFS spectra of $La_{1-x}Sr_xMnO_{3-\delta}$ at Mn L_3-edge and L_2-edge. (c) k^2-weighted R-space EXAFS spectra of $La_{1-x}Sr_xMnO_{3-\delta}$ at Mn K-edge. (d) k^2-weighted R-space EXAFS spectra of $La_{1-x}Sr_xMnO_{3-\delta}$ at Sr K-edge. (e) Schematic energy level diagram of Mn^{4+} and Mn^{3+} with weak and strong Jahn-Teller effect. Crystal field splitting, exchange splitting and J.T. splitting are listed as Δ_O, Δ_{ex} and Δ_J. J.T. effect in Mn^{3+} split the e_g into d_{x2-y2}, d_{z2}, and t_{2g} into d_{xy}, d_{xz} and d_{yz}. (f) NEXAFS spectra of $La_{1-x}Sr_xMnO_{3-\delta}$ at O K-edge. In full range O K-edge NEXAFS spectra (Supplementary Fig. 7), Absorption peaks at 529.6 eV, 536.0 eV and 543.8eV, attributed to the hybridisation between O 2p orbitals and Mn 3d, La 5d / Sr 4d and Mn 4s,p / La 6s,p / Sr 5s,p orbitals, respectively. (g) Plot of O K-edge peak FWHM (red) and conductivity (black) as a function of Sr doping amount. The FWHM results are calculated from peak fitting of O K-edge NEXAFS (Supplementary Fig. 8) and are listed in Supplementary Table 3. The conductivity is tested by 4-point probe method. (h) Plot of conductivity as a function of O K-edge peak FWHM.

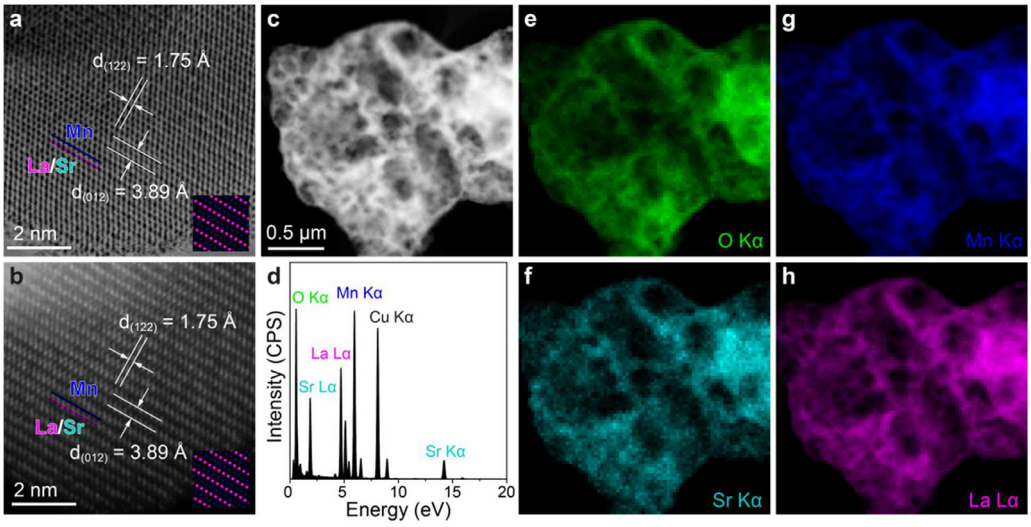

Fig. 3. STEM image and EDS mapping of LSMO-0.3. (a) BF-STEM image and (b) HAADF-STEM image. The d-spaces of (122) and (012) facets are identified as 1.75 Å and 3.89 Å, respectively. (c) HAADF-STEM image at large scale and (d) corresponding EDS spectra of the whole area. (e-h) EDS element mapping at the same area of (e) O Kα emission, (f) Sr Kα emission, (g) Mn Kα emission and (h) La Lα emission.

from 12.55 S cm^{-1} to 28.61 S cm^{-1} from 0.1 Sr^{2+} to 0.3 Sr^{2+} and then decreases to 25.33 S cm^{-1} at 0.5 Sr^{2+} (Fig. 2g black). A negative correlation is found between the conductivity and the FWHM of the O 1s to Mn 3d e_g ↑ and t_{2g} ↓ transition (Fig. 2h). The $La_{0.7}Sr_{0.3}MnO_{3-\delta}$ (LSMO-0.3) has the highest conductivity due to the desired Mn^{3+}/Mn^{4+} ratio and the least Jahn-Teller distortion of the MnO_6 octahedrons [45]. This excellent conductivity of LSMO-0.3 also changes the kinetic of redox reaction of sulfur. When the conductivity increased from 0.15 S cm^{-1} of LMO layer to 28.61 S cm^{-1} of LSMO-0.3 layer, the potential of anodic peak decreased by 0.14 V, and related two cathodic peaks have increased potential from LMO to LSMO-0.3 (Supplementary Fig. 9). The lower anodic peaks and higher cathodic peaks of LSMO-0.3 show better kinetic of redox reaction comparing to the LMO's.

The lattice fringes are clearly visible in the BF-STEM andHAADF-STEM images (Fig. 3a,b). The La/Sr and Mn layer are clearly visible with the lattice fringes of 1.75 and 3.89 Å for (122) and (012) facets, respectively. The energy dispersive X-ray spectroscopy (EDS) shows features for La Lα, Sr Kα, Lα, and Mn Kα emissions. The corresponded element maps show the uniform distribution of La, Sr, Mn, and O (Fig. 3c-3h). Nitrogen physisorption measurements also reveal that LSMO-0.3 has a porous structure with a specific surface area of 14 m^2 g^{-1} (Supplementary Fig. 10). The aforementioned XAFS and STEM analysis studies the effect of Sr-doping with atomic accuracy, providing structure evidence for the improved electron hopping conduction, which will result in enhancing the function of LSMO modified separator.

3.3. The function of $La_{1-x}Sr_xMnO_{3-\delta}$ separator

The adsorption of lithium polysulfides is shown by the colour change of Li_2S_4 solution upon the addition of LSMO samples (Supplementary Fig. 11). When the Sr content *x* is between 0.2 and 0.5, an almost colourless solution is achieved. To further verify the adsorption rate and capacity, we design the high concentration of Li_2S_4 solution of 2 mg mL^{-1} as the standard solution, and the ratio of active mass (LMO and LSMO-0.3) to Li_2S_4 solution maintain 10 mg mL^{-1}. Then we observe the changes of Li_2S_4 solution colour every one hour to evaluate the adsorption rate and capacity. The fresh solution with both LMO and LSMO-0.3 is yellow colour and the LSMO-0.3 solution turn colourless after 5 h. In contrast to LSMO-0.3, the colour r of LMO solution need 16 h to turn colourless. (Supplementary Fig. 12) So the sorption rate of LSMO-0.3 is more than three times of the LMO's. The adsorption of the Li_2S_4 can be understood as the chemical interactions between S_4^{2-} and $Mn^{3+/4+}$ pair in the previous paper [47]. To confirm the interaction between Mn cations and polysulfides, we measured the XPS spectra of La, Sr and Mn in LSMO-0.3 and LSMO-0.3/Li_2S_4 (Supplementary Fig. 13). The peaks of Mn 2p spectra shift to lower binding energy revealing the chemical interaction between Mn cations and polysulfides. Combining the high electron hopping conduction and polysulfides adsorption ability. the LSMO-0.3 is chosen to coat on the surface of the Celgard separator with a thickness of ~7 μm (Supplementary Fig. 14 and 15). X-ray micro-CT was used to validate the design concept of LSMO-0.3 functionalized separator *via* observation of the microstructural changes of cathode, functional membrane, and separator. An as-prepared sulfur electrode, the LSMO-0.3 modified separator and Li foil were assembled in a bespoke 1/8-inch Swagelok cell (Fig. 1c). Such Swagelok cell has been proven to be feasible for the X-ray CT analysis, and the performance decay is similar to that of coin cell [38,40]. The virtual slices obtained from the tomograms of the pristine cell and the same cell after 10 cycles at a 0.1 C rate (both acquired at full state of charge) demonstrate the changes occurring within the cathode structure (Fig. 4). The front view virtual slice of the pristine cell shows the uniform dispersion of sulfur within the ~50 μm thick cathode, where a ~7 μm thick LSMO-0.3 layer (Fig. 4a) can be visualized on top of the cathode. The red dots in the cathode layer are the sulfur particles, which are uniformly distributed in the pristine cell. The yellow islands represent assembly of primary sulfur particles into large aggregates. Those aggregates are possibly formed during the synthesis of cathode materials, or during the assembly of the cathode [39,40]. Only very few of them are found in the pristine cell, located in both the cathode and cathode/LSMO interface. The size and dispersion of sulfur particles and aggregates are further revealed by cross-sectional virtual slices (Fig. 4b). Cycling at a current equivalent to a 0.1 C rate for 10 cycles, the sulfur particles enrich at the cathode/ LSMO interface and have reduced intensity at the cathode/current collector interface (Fig. 4f). The amount of the sulfur aggregates significantly increases after 10 cycles (yellow in Fig. 4f). A dense layer is formed at the cathode/ LSMO interface, with a few aggregates scatter throughout the other locations in the cathodes. Such redistribution of sulfur is also seen in the comparison of the cross-sectional virtual slices between the cell (Fig. 4b) and cycled cell (Fig. 4g). The same changes can also be seen in the front view virtual slices (Supplementary Fig. 16 and 17). The proposed mechanism behind these observations is: 1) Aggregation from primary sulfur particles into aggregates; 2) a collective movement of sulfur particles and aggregates from the cathode in the direction of the anode caused by the shuttling of lithium polysulfide species; and 3) the successful shielding of these sulfur particles at both cathode/LSMO-0.3 membrane interface and separator/LSMO-0.3 layer interface. This imaging study shows that the aggregation of sulfur is inevitable but LSMO-0.3 captures and shields polysulfides, preventing their migration from cathode to the anode.

The transmission of X-ray is then quantified in the 2D radiographs of the pristine and cycled cells (Fig. 4c,h). A magnified region-of-interest image, bound by the yellow dashed box, was selected to obtain a line profile of X-ray transmission (Fig. 4d,i). Less X-ray transmission in the linear scan curves will be observed if the X-ray scanning location has an enrichment of sulfur particles. A decrease of transmission from ~10% to 8% is observed at the LSMO-0.3 layer from pristine cell to cycled cell (Fig. 4e,j), due to the adsorption of polysulfide species. The same phenomenon is also observed on the separator/LSMO-0.3 and cathode/LSMO-0.3 interfaces, showing a general enrichment of sulfur around LSMO-0.3 instead of random diffusion across the whole separator. The transmission of cathode far position (cathode/current collector interface) in cycled cell is higher than that in the pristine cell, indicating the reduced sulfur content in the cycled cell than that in the pristine cell, which is in good agreement with the above-mentioned reconstructed virtual slices (Fig. 4a,f). The X-ray CT study thus validates the sulfur shielding function and the adsorption ability of the LSMO-0.3 membrane during the charge and discharge process.

3.4. The cell performance with $La_{1-x}Sr_xMnO_{3-\delta}$ separator

XAFS and X-ray CT study determines the structural changes upon Sr^{2+} doping, the origin of high conductivity and the sulfur shielding function. In the LSMO (Sr=0-0.5) system, the LSMO-0.3 has the highest conductivity of 28.61 S cm^{-1} (Fig. 2g) and strong adsorption. So the Li-S battery equipped with the LSMO-0.3 functionalized separator is then assembled to reveal the overall improvement of the storage capacity. In the cyclic voltammogram (CV) at a scan rate of 0.05 mV s^{-1}, the cathodic peaks located at ~2.30 and 2.05 V is identified, corresponding to the reduction reaction of S_8 to high-order polysulfides (Li_2S_x, x = 4-8), and then to low-order Li_2S_2/Li_2S, respectively (Fig. 5a). In the subsequent anodic process, two oxidation peaks are observed at ~2.35 and 2.40 V, which relate to the reverse reaction of Li_2S_2/Li_2S to higher-order polysulfides (Li_2S_x, x= 4-8), then to S, respectively. The voltage-capacity curves show two discharge plateaus located at ~2.30 and 2.05 V, and two adjacent charge plateaus at ~2.30 and 2.40 V, which are in good agreement with the CV results (Fig. 5b). The rate performance of the cell with LSMO-0.3 membrane reveals a reversible capacity of 1346, 1187, 1014, 916 and 802 mAh g^{-1} at 0.1, 0.2, 0.5, 1 and 2 C, respectively, which is much higher than the cell with a $LaMnO_3$ (LMO) membrane, and the cell without any functional membrane. When the C-rate is reset back to 0.1 C after running at various rates, a reversible capacity of 1188 mAh g^{-1} is recovered, corresponding to a capacity retention of 88.3% (Fig. 5c). Such an exceptional rate performance of the cell with the LSMO-0.3 membrane is ascribed to the high electronic conductivity with Sr-doping. At 0.5 C rate and during the initial 10 charge and discharge cycles, the capacity of cell without LSMO-0.3 layer decreases rapidly from 1046 to 798 mAh g^{-1}, which is much faster than the cell with LSMO-0.3 layer (from 1138 to 1089 mAh g^{-1}, Fig. 5d). On one hand, the X-ray CT study visualizes the sulfur shielding for the LSMO-0.3 layer, maintaining the majority of the sulfur within cathode, whereas the cell without LSMO-0.3 layer suffers from major sulfur loses in our previous study [48,49]. On the other hand, such LSMO-0.3 layer significantly improves the initial cycling performance from 248 mAh g^{-1} to only 49 mAh g^{-1} decay. The combination of the X-ray CT, visual adsorption experiment and cycling performance validates our hypothesis on the shielding effect of the LSMO and its ability to reactivating inactive deposits of sulfur-containing species. The capacity of LMO layer is between LSMO free and LSMO-0.3 layer cells. This is attributed to the weak electronic conductivity of the LMO, providing the physical shielding and low chemical adsorption of polysulfides. In the long-term cycling tests, the cell with the LSMO-0.3 membrane achieves an initial capacity of 1138 mAh g^{-1} and maintains 675 mAh g^{-1} after 400 cycles (0.5 C), corresponding to a capacity fade of only 0.1% per cycle (Fig. 5d). This result is indicative of excellent capacity retention and cycle stability. In addition, the Coulombic efficiency (CE) of the cell is stabilized at > 99% during long-term cycling. Moreover, the capacity fade of 0.12% with LSMO-0.3 layer is lower than that of 0.14% with

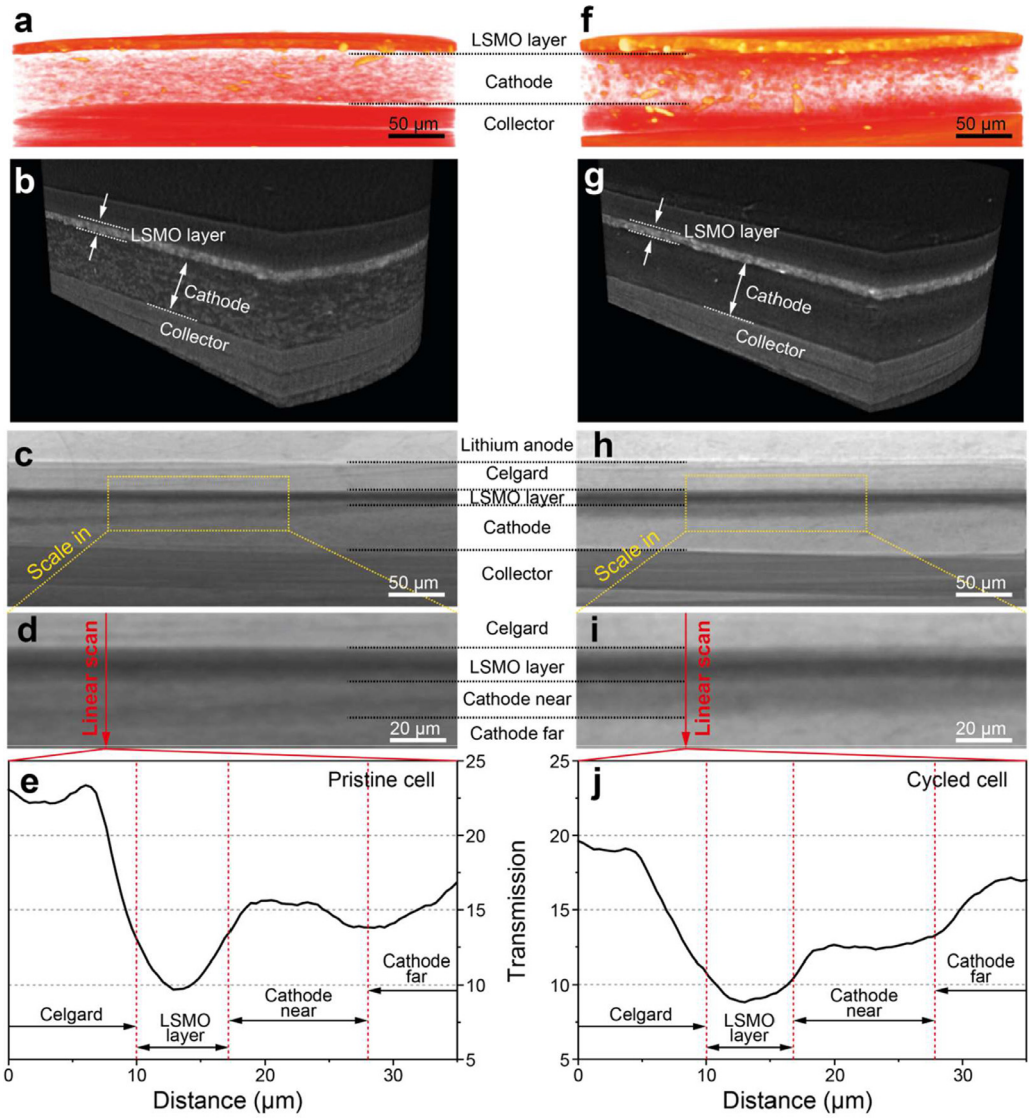

Fig. 4. (a) 3D reconstructed volumes of pristine cell. Red dots: primary sulfur particles; yellow islands: assembly of primary sulfur particles into large aggregates. (b) 3D cross-sectional virtual slices of pristine cell. (c) 2D radiographs of pristine cell. (d) Magnified region-of-interest image from (c) and (e) corresponding linear scan of X-ray transmission. (f) 3D reconstructed volumes of the same cell after 10 cycles. (g) 3D cross-sectional virtual slices of the same cell after 10 cycles. (h) 2D radiographs of the same cell after 10 cycles. (i) Magnified region-of-interest image from (h) and (j) corresponding linear scan of X-ray transmission.

LMO and 0.16% with pure sulfur (bare Celgard separator) in the first 200 cycles in Fig. 5d. The shielding effect of the functional membrane was investigated by comparing the self-discharge behaviours of LSMO-0.3, LMO, and pure sulfur cells (Fig. 5e-g). All cells were run at 0.2 C for 7 cycles (C^{7th}), then held at 2.1 V during the 8th discharge (C^{8th}) for 3 days before resuming discharge. Discharge capacity of the cell with LSMO-0.3 membrane drops from 1197 to 1152 mAh g^{-1}, corresponding to 3.76% self-discharge rate according to $(C^{7th}\text{-}C^{8th})/C^{7th} \times 100\%$ (Fig. 5e). In comparison, 7.71% and 12.05% rates are observed for cell with LMO membrane and with no membrane, respectively (Fig. 5f,g). The self-discharge is mainly due to the diffusion of Li_2S_x, which is successfully suppressed with the LSMO-0.3 membrane.

Sulfur loading is one of the key factors determining the actual energy density of Li-S batteries. The electrochemical performance of the battery usually deteriorates with increasing S loading. Towards realistic conditions in commercial cells, S loading is increased from 3.1 to 8.4 mg_{sulfur} cm^{-2} to evaluate the high energy performance of cells containing the LSMO-0.3 membrane. All the cathodes achieve a reversible specific capacity of about 1000 mAh g^{-2} at 0.1 C, showing high S utilization (Fig. 6a). Compared with the low sulfur loading cell (3.1 mg cm^{-2}), the high loading cell achieve similar reversible specific capacity but with a much higher areal specific capacity (Fig. 6b,c). In addition, the areal capacity and corresponding Coulombic efficiency at 0.1 C rate also show good cyclability regardless of sulfur loading (Fig. 6d). A long-term cycling test was performed for an electrode with a 6.9 mg_{sulfur} cm^{-2} loading (Fig. 6e). The initial capacity is 932 mAh g^{-1}, with a reversible capacity that stabilized at 370 mAh g^{-1} and 2.6 mAh cm^{-2} after 300 cycles, showing outstanding cycle stability with only 0.2% capacity fade per cycle. Together with the XAFS and X-ray CT study, we demonstrate here that the Sr^{2+} doping at the atomic scale can significantly improve the conductivity and shielding effect of the LSMO membrane, leading to superior performance of the Li-S cell with very high sulfur loadings. If the scientists want to further enhance the LSMO effect, it is suitable to design the combined cathode with LSMO and carbon in nano-scale structure as core-shell (LSMO-carbon) or a multi-layered structure, which should improve the electrochemical performance.

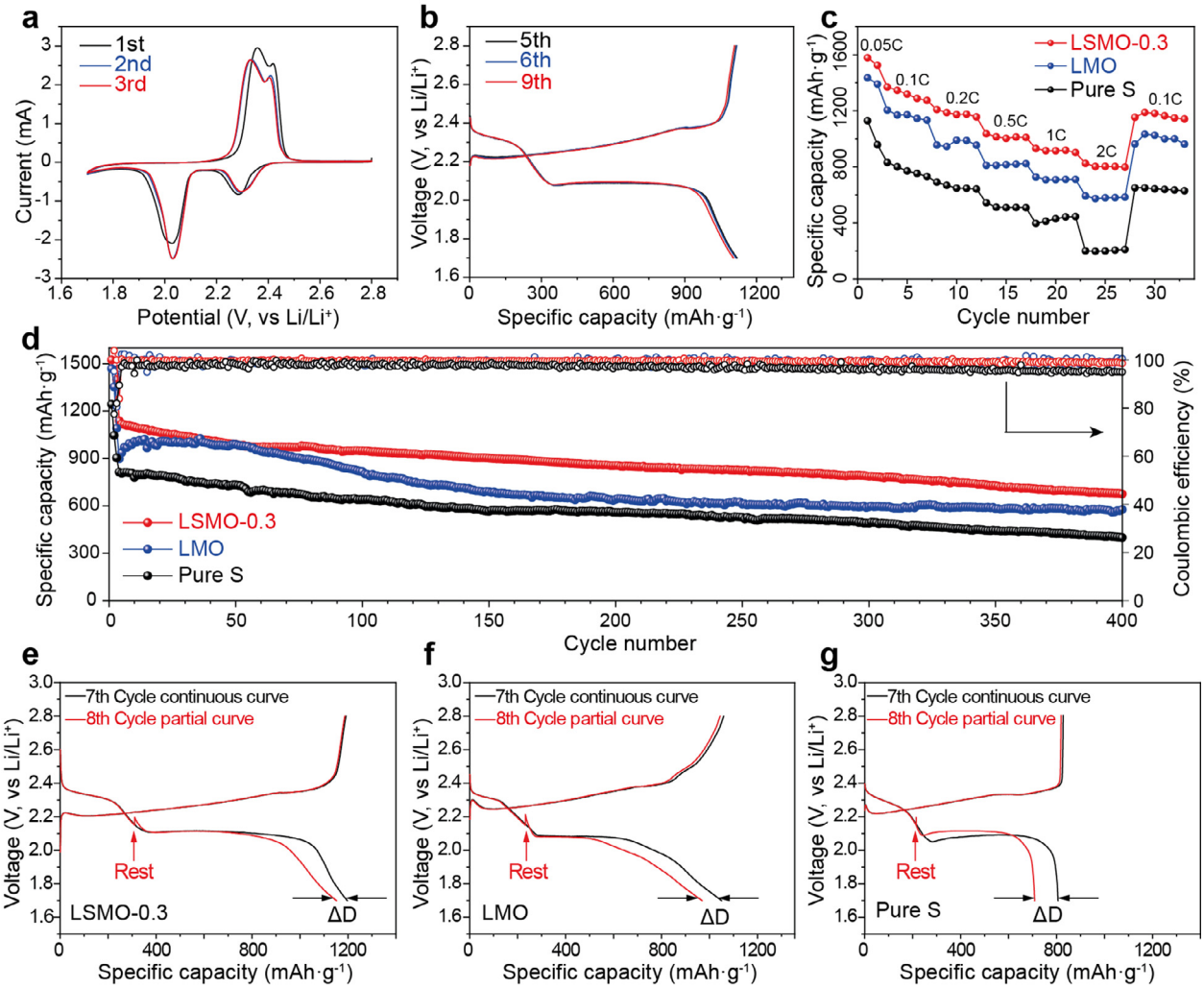

Fig. 5. (a) CV curves of the cell with LSMO-0.3 modified membrane between 1.7 and 2.8 V. (b) Charge and discharge profiles of the cell with LSMO-0.3 modified membrane at 0.5 C for the 5th, 6th and 9th cycles. (c) Rate performance of cells with different membranes at the rates from 0.1 to 2 C rate. (d) Cycling performance and corresponding Coulombic efficiency based on pure sulfur, LMO membrane and LSMO-0.3 membrane cells. (e) Self-discharge tests of LSMO-0.3 membrane cells. (f) Self-discharge tests of LMO membrane cells. (g) Self-discharge tests of pure sulfur cells. The current of (e-g) is 0.2 C rate.

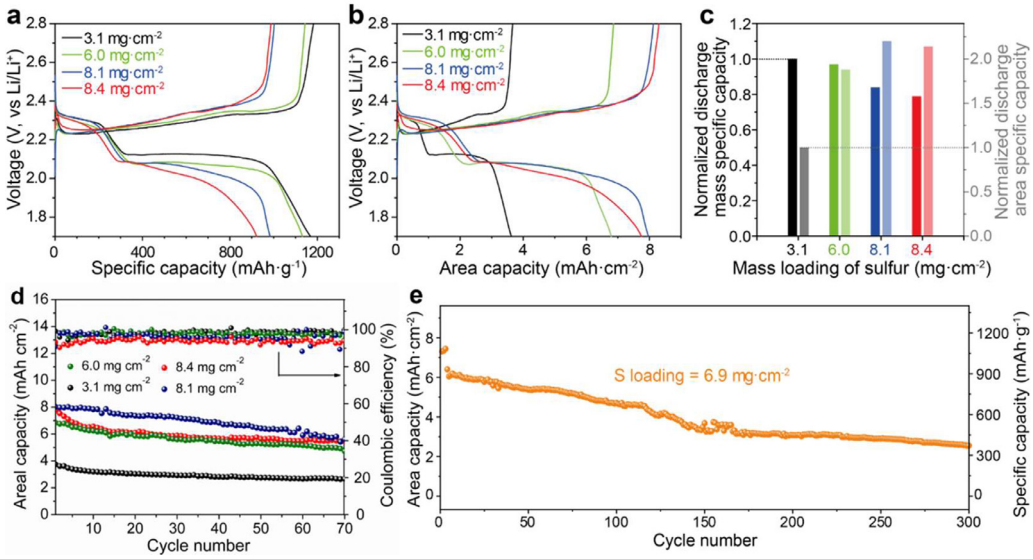

Fig. 6. Effects of S loading for cells with LSMO-0.3 membrane. (a) Voltage *vs.* specific capacity profiles at 0.1 C with various sulfur loadings. (b) Voltage *vs.* areal capacity profiles at 0.1 C with various sulfur loadings. (c) Comparison of areal discharge capacity and gravimetric specific capacity of different sulfur loadings. (d) Areal capacity and corresponding Coulombic efficiency at 0.1 C. (e) Cycling performance of the high loading cell with 6.9 mg_{sulfur} cm^{-2} at 0.2 C.

4. Conclusions

In summary, considering the high electron hopping conduction and polysulfide adsorption effect, we have designed an LSMO-0.3 modified separator in Li-S system. The doping of Sr^{2+} leads to the partial oxidation of Mn^{3+} to Mn^{4+} and coordination environment change, which not only improves electronic conductivity but also facilitates the adsorption interaction between Mn cations and polysulfides. The origin of high conductivity, the *in situ* role of polysulfides shielding, and the high sulfur loading battery performance are investigated through a consecutive multiscale analysis. Our study reveals how the structural geometric changes of Sr-doping at atomic scale analysed via XAFS technique can greatly improve its function at microscopic scale visualized through X-ray CT and finally leading to superior electrochemical performance.

Declaration of Competing Interest

The authors declare no competing interests.

CRediT authorship contribution statement

Zhangxiang Hao: Conceptualization, Investigation, Methodology, Writing – original draft, Writing – review & editing. **Jie Chen:** Data curation, Methodology, Writing – review & editing. **Xuekun Lu:** Data curation, Formal analysis. **Liqun Kang:** Data curation, Formal analysis. **Chun Tan:** Data curation, Formal analysis. **Ruoyu Xu:** Data curation, Formal analysis. **Lixia Yuan:** Funding acquisition, Project administration, Supervision. **Dan J.L. Brett:** Funding acquisition, Project administration, Software. **Paul R. Shearing:** Funding acquisition, Project administration, Software. **Feng Ryan Wang:** Funding acquisition, Project administration, Supervision, Writing – original draft, Writing – review & editing. **Yunhui Huang:** Funding acquisition, Project administration, Supervision, Writing – original draft.

Acknowledgments

The project is funded by EPSRC (EP/P02467X/1 and EP/S018204/2) and the Centre for Nature Inspired Chemical Engineering (EP K038656/1), and the National Science Foundation of China (Grant Nos. 51532005 and U1764256). We acknowledge B18 Beamline of Diamond Light Source (DLS) and E01 beamline of the electron Physical Science Imaging Centre (ePSIC) for the beamtime (session ID: SP19072 and EM19246, respectively). We acknowledge ISISS beamline at BESSY II of Helmholz-Zentrum Berlin for the beamtime (proposal ID: 18207435-ST). The authors acknowledge the Analytical and Testing Center of Huazhong University of Science and Technology for XRD and FESEM.

Supplementary materials

Supplementary material associated with this article can be found, in the online version, at doi:10.1016/j.ensm.2022.04.003.

References

[1] Q. Pang, X. Liang, C.Y. Kwok, L.F. Nazar, Nat. Energy 1 (2016) 16132.
[2] H.-J. Peng, J.-Q. Huang, X.-B. Cheng, Q. Zhang, Adv. Energy Mater. 7 (2017) 1700260.
[3] C. Li, R. Liu, Y. Xiao, F. Cao, H. Zhang, Energy Storage Mater. 40 (2021) 439–460.
[4] D. Su, D. Zhou, C. Wang, G. Wang, Adv. Funct. Mater. 28 (2018) 1800154.
[5] J.Q. Huang, Q. Zhang, F. Wei, Energy Storage Mater. 1 (2015) 127–145.
[6] J. Zhang, H. Hu, Z. Li, X.W. Lou, Angew. Chem. Int. Ed. 55 (2016) 3982–3986.
[7] Y. Sun, N. Liu, Y. Cui, Nat. Energy 1 (2016) 16071.
[8] Z. Fan, C. Zhang, W. Hua, H. Li, Y. Jiao, J. Xia, C. Geng, R. Meng, Y. Liu, Q. Tang, Z. Lu, T. Shang, G. Ling, Q. Yang, J. Energy Chem. 62 (2021) 590–598.
[9] M. Wild, L. O'Neill, T. Zhang, R. Purkayastha, G. Minton, M. Marinescu, G.J. Offer, Energy Environ. Sci. 8 (2015) 3477–3494.
[10] A. Du, Z. Zhang, H. Qu, Z. Cui, L. Qiao, L. Wang, J. Chai, T. Lu, S. Dong, T. Dong, H. Xu, X. Zhou, G. Cui, Energy Environ. Sci. 10 (2017) 2616–2625.
[11] M. Zhao, Y.-Q. Peng, B.-Q. Li, X.-Q. Zhang, J.-Q. Huang, J. Energy Chem. 56 (2021) 203–208.
[12] H. Yuan, H.-J. Peng, B.-Q. Li, J. Xie, L. Kong, M. Zhao, X. Chen, J.-Q. Huang, Q. Zhang, Adv. Energy Mater. 9 (2019) 1802768.
[13] W. Cai, G. Li, F. He, L. Jin, B. Liu, Z. Li, J. Power Sources 283 (2015) 524–529.
[14] Z.X. Hao, L.X. Yuan, Z. Li, J. Liu, J.W. Xiang, C. Wu, R. Zeng, Y.H. Huang, Electrochim. Acta 200 (2016) 197–203.
[15] T.Z. Zhuang, J.Q. Huang, H.J. Peng, L.Y. He, X.B. Cheng, C.M. Chen, Q. Zhang, Small 12 (2016) 381–389.
[16] J. Balach, T. Jaumann, M. Klose, S. Oswald, J. Eckert, L. Giebeler, Adv. Funct. Mater. 25 (2015) 5285–5291.
[17] H. Gao, S. Ning, J. Lin, X. Kang, Energy Storage Mater. 40 (2021) 312–319.
[18] J.-Q. Huang, Q. Zhang, H.-J. Peng, X.-Y. Liu, W.-Z. Qian, F. Wei, Energy Environ. Sci. 7 (2014) 347–353.
[19] H.J. Peng, D.W. Wang, J.Q. Huang, X.B. Cheng, Z. Yuan, F. Wei, Q. Zhang, Adv. Sci. 3 (2016) 1500268.
[20] G. Zhou, L. Li, D.W. Wang, X.Y. Shan, S. Pei, F. Li, H.M. Cheng, Adv. Mater. 27 (2015) 641–647.
[21] F. Zeng, Z. Jin, K. Yuan, S. Liu, X. Cheng, A. Wang, W. Wang, Y.-s. Yang, J. Mater. Chem. A 4 (2016) 12319–12327.
[22] F. Liu, Q. Xiao, H.B. Wu, F. Sun, X. Liu, F. Li, Z. Le, L. Shen, G. Wang, M. Cai, Y. Lu, ACS Nano 11 (2017) 2697–2705.
[23] W. Li, J. Hicks-Garner, J. Wang, J. Liu, A.F. Gross, E. Sherman, J. Graetz, J.J. Vajo, P. Liu, Chem. Mater. 26 (2014) 3403–3410.
[24] C.-X. Zhao, X.-Y. Li, M. Zhao, Z.-X. Chen, Y.-W. Song, W.-J. Chen, J.-N. Liu, B. Wang, X.-Q. Zhang, C.-M. Chen, B.-Q. Li, J.-Q. Huang, Q. Zhang, J. Am. Chem. Soc. 143 (2021) 19865–19872.
[25] J. Liu, L. Yuan, K. Yuan, Z. Li, Z. Hao, J. Xiang, Y. Huang, Nanoscale 8 (2016) 13638–13645.
[26] X. Wang, G. Li, J. Li, Y. Zhang, A. Wook, A. Yu, Z. Chen, Energy Environ. Sci. 9 (2016) 2533–2538.
[27] Z. Hao, R. Zeng, L. Yuan, Q. Bing, J. Liu, J. Xiang, Y. Huang, Nano Energy 40 (2017) 360–368.
[28] L. Kong, X. Chen, B. Li, H. Peng, J. Huang, J. Xie, Q. Zhang, Adv. Mater. 30 (2018) 1705219.
[29] Y. Song, W. Zhao, L. Kong, L. Zhang, X. Zhu, Y. Shao, F. Ding, Q. Zhang, J. Sun, Z. Liu, Energy Environ. Sci. 11 (2018) 2620–2630.
[30] J. Pu, Z. Shen, J. Zheng, W. Wu, C. Zhu, Q. Zhou, H. Zhang, F. Pan, Nano Energy 37 (2017) 7–14.
[31] Z. Xiao, Z. Yang, L. Wang, H. Nie, M. Zhong, Q. Lai, X. Xu, L. Zhang, S. Huang, Adv. Mater. 27 (2015) 2891–2898.
[32] M.U. Patel, R. Demir-Cakan, M. Morcrette, J.M. Tarascon, M. Gaberscek, R. Dominko, ChemSusChem 6 (2013) 1177–1181.
[33] C. Barchasz, F. Molton, C. Duboc, J.C. Lepretre, S. Patoux, F. Alloin, Anal. Chem. 84 (2012) 3973–3980.
[34] T. Yim, S.H. Han, N.H. Park, M.-S. Park, J.H. Lee, J. Shin, J.W. Choi, Y. Jung, Y.N. Jo, J.-S. Yu, K.J. Kim, Adv. Funct. Mater. 26 (2016) 7817–7823.
[35] P.R. Shearing, Nat. Energy 1 (2016) 16173.
[36] X. Lu, T. Li, A. Bertei, J.I.S. Cho, T.M.M. Heenan, M.F. Rabuni, K. Li, D.J.L. Brett, P.R. Shearing, Energy Environ. Sci. 11 (2018) 2390–2403.
[37] T. Li, T.M.M. Heenan, M.F. Rabuni, B. Wang, N.M. Farandos, G.H. Kelsall, D. Matras, C. Tan, X. Lu, S.D.M. Jacques, D.J.L. Brett, P.R. Shearing, M. Di Michiel, A.M. Beale, A. Vamvakeros, K. Li, Nat. Commun. 10 (2019) 1497.
[38] S.R. Daemi, X. Lu, D. Sykes, J. Behnsen, C. Tan, A. Palacios-Padros, J. Cookson, E. Petrucco, P.J. Withers, D.J.L. Brett, P.R. Shearing, Mater. Horiz. 6 (2019) 612–617.
[39] F. Sun, M. Osenberg, K. Dong, D. Zhou, A. Hilger, C.J. Jafta, S. Risse, Y. Lu, H. Markötter, I. Manke, ACS Energy Lett 3 (2018) 356–365.
[40] C. Tan, T.M.M. Heenan, R.F. Ziesche, S.R. Daemi, J. Hack, M. Maier, S. Marathe, C. Rau, D.J.L. Brett, P.R. Shearing, ACS Appl. Energy Mater. 1 (2018) 5090–5100.
[41] C. Tan, M.D.R. Kok, S.R. Daemi, D.J.L. Brett, P.R. Shearing, Phys. Chem. Chem. Phys. 21 (2019) 4145–4154.
[42] F. Studer, O. Toulemonde, V. Caignaert, P. Srivastava, J.B. Goedkoop, N.B. Brookes, J. Phys. IV 7 (1997) 529–530.
[43] O. Toulemonde, F. Studer, A. Llobet, L. Ranno, A. Maignan, E. Pollert, M. Nevriva, E. Pellegrin, N.B. Brooks, J. Goedkoop, J. Magn. Magn. Mater. 190 (1998) 307–317.
[44] O. Toulemonde, F. Studer, A. Barnabe, B. Raveau, J.B. Goedkoop, Eur. Phys. J. B 18 (2000) 233–240.
[45] H. Kamata, J. Phys. Chem. Solids 56 (1995) 943–955.
[46] R.M. Qiao, T. Chin, S.J. Harris, S.S. Yan, W.L. Yang, Curr. Appl. Phys. 13 (2013) 544–548.
[47] X. Liang, C.Y. Kwok, F. Lodi-Marzano, Q. Pang, M. Cuisinier, H. Huang, C.J. Hart, D. Houtarde, K. Kaup, H. Sommer, T. Brezesinski, J. Janek, L.F. Nazar, Adv. Energy Mater. 6 (2016) 1501636.
[48] R. Xu, J. Xiang, J. Feng, X. Lu, Z. Hao, L. Kang, M. Li, Y. Wu, C. Tan, Y. Liu, G. He, D. Brett, P. Shearing, L. Yuan, Y. Huang, F. Wang, Energy Storage Mater. 31 (2020) 16–171.
[49] A. Yermukhambetova, C. Tan, S.R. Daemi, Z. Bakenov, J.A. Darr, D.J.L. Brett, P.R. Shearing, Sci Rep. 6 (2016) 35291.